Sensitivity Analysis in High-Frequency Modeling of Traction Motors with Hairpin Windings

Silvan Scheuermann
Institute of Electrical Engineering (ETI)
Karlsruhe Institute of Technology (KIT)
Karlsruhe, Germany
silvan.scheuermann@kit.edu

Matthias Brodatzki
Institute of Electrical Engineering (ETI)
Karlsruhe Institute of Technology (KIT)
Karlsruhe, Germany
matthias.brodatzki@kit.edu

Martin Doppelbauer
Institute of Electrical Engineering (ETI)
Karlsruhe Institute of Technology (KIT)
Karlsruhe, Germany
martin.doppelbauer@kit.edu

***Abstract*—The shift towards electrified mobility has accelerated the deployment of fast-switching semiconductors, such as silicon carbide (SiC) and gallium nitride (GaN), in power electronics. While these semiconductors enhance the systems' efficiency, they pose new challenges due to high-frequency interferences with electric drives, such as insulation stress and bearing currents. Accurate high-frequency impedance models are a valuable tool for predicting these effects, but their validity and predictive accuracy depend substantially on precise parameterization. Developing such models often necessitates simplifications and assumptions to maintain computational feasibility. However, many models in the literature often do not account for critical factors such as the presence of the rotor or fail to validate their omissions. This paper investigates the impact of key simplifications on model accuracy, aiming to establish the limits of their validity.**

***Index Terms*—High-frequency motor model, Parameterization influence, Traction motor, Hairpin winding, Electric stress**

I. Introduction

The development of high-frequency (HF) models to predict the transient voltage distribution and parasitic HF-effects in electric machines has gained more attention due to the increasing use of SiC- and GaN-semiconductors in inverter systems for traction applications. The higher switching frequencies and steeper voltage edges associated with these technologies, along with the pulse width modulation (PWM) technique necessitate more precise modeling of HF-effects. These inverter-related characteristics can result in undesirable HF-phenomena such as electromagnetic interference (EMI), bearing currents or increased insulation stress [1].

Existing models in the literature vary in scope, with some covering not only the electric machine but also taking the power electronics, cabling, or even the entire drive system into account [2]. Most of the models are composed of electrical circuits that include a variety number of resistances, inductances, and capacitances. The parameterization of these electrical elements is derived either by measurement-based fitting, Finite Element Methods (FEM), analytical approaches or by hybrid methods [1], [3]–[5]. However, the accuracy and validity of these models are often constrained by high computational effort, as fully detailed 3D models are required for optimal precision.

In developing HF models for automotive traction motors, focusing on transient voltage distribution and associated parasitic HF-effects, several critical simplifications and assumptions commonly used in the literature were identified as significantly affecting the models' parameterization and thus the accuracy.

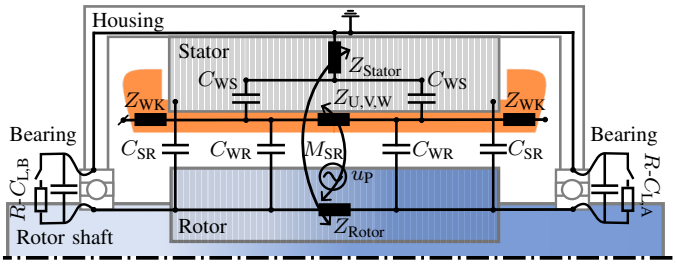

Fig. 1: Overall structure of the HF-motor model

The previous study [6] investigated the influence of factors such as the analysis current, rotor presence and rotor magnets as well as its angle dependency. In contrast, this paper provides a sensitivity analysis aimed to uncover the impact of such assumptions and simplifications, furthermore to define the limits of their validity.

Accordingly, Section II briefly outlines the own modeling approach and the parameterization of the elements. In Section III the validation of the model is given, serving as fundamental base for the sensitivity analysis in Section IV. The study refers to a three-phase 245 kW hairpin-wound internal permanent magnet motor with 48 slots and six conductors per slot.

II. High-Frequency Model

The own developed HF-equivalent circuit model is shown in Fig. 1. It is classified as a lumped parameter model that represents the entire motor structure and its HF-behavior using resistances, inductances, and capacitances. Since the winding is the primary focus in HF-models, it is treated as a sub-model, with the stator core part only represented in simplified form by $Z_{\mathrm{U,V,W}}$ and the end-winding regions by Z_{WK} in Fig. 1.

In addition, the capacitive and inductive paths of the rotor and the impedance behavior of the motor's bearings are modeled. The capacitances between the winding and the stator C_{WS}, between the winding and the rotor C_{WR} and between the stator and the rotor C_{SR} are divided into two parallel branches for symmetry reasons.

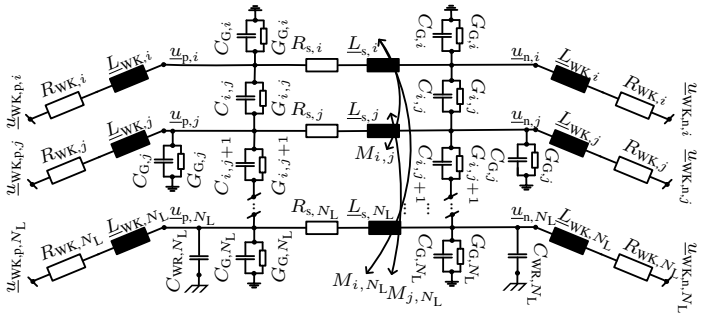

Fig. 2: Lumped parameter modeling of one slot with N_L coil sides

A detailed description of the motor model's components and corresponding electrical elements is provided in the following.

A. Winding

The detailed sub-model of the winding, initially represented by $Z_\mathrm{U,V,W}$ and Z_WK, is illustrated in Fig. 2 and can be described as a slot- and layer-domain lumped parameter model.

In this model, each of the N_N slots contains N_L coil sides, which are characterized by frequency-dependent resistances $R_{\mathrm{s},i}$, complex self-inductances $\underline{L}_{\mathrm{s},i}$, as well as their $(N_\mathrm{N} \times N_\mathrm{L}) \times [(N_\mathrm{N} \times N_\mathrm{L}) - 1]$ mutual couplings $M_{i,j}$.

The capacitances $C_{\mathrm{G},i}$ are used to describe the electric field across the insulation material to the stator core, while $C_{i,j}$ represent the electric fields between adjacent conductors. The parallel conductances $G_{\mathrm{G},i}$ and $G_{i,j}$ are introduced to account for the dissipative power loss in insulation materials when subjected to an alternating electric field.

The overhang regions of the motor Z_WK are modeled in Fig. 2 by R_WK-$\underline{L}_\mathrm{WK}$ elements and are connected to the slot part of each coil-side. Capacitances, associated parallel conductances, and inductive couplings in the end-winding regions are neglected in the final model due to their minimal influence compared to the laminated stator core. This assumption is supported by e.g. [7] and will be further investigated in Section IV-A.

B. Stator

In the comprehensive motor model depicted in Fig. 1, the high-frequency common-mode (CM) flux is modeled using the transformer model according to [8], incorporating the impedances $\underline{Z}_\mathrm{Stator}$ and $\underline{Z}_\mathrm{Rotor}$, along with their mutual coupling $\underline{M}_\mathrm{SR}$.

These impedances are essential for modeling the HF-CM flux induced by CM currents in each individual lamination sheet of the stator core over its entire length. As these currents flow in a meandering pattern through the laminated core, the interaction of the currents between different lamination sheets must also be taken into account. A detailed explanation of this phenomenon can be found in [9]–[11].

C. Rotor

A key extension in this HF model is the introduction of the back-electromotive force (EMF) by the element u_P. This addition allows for the inclusion of operating-point dependencies by accounting for the voltage induced by the rotor. The impact on the results of considering versus neglecting Back-EMF is examined in Section IV-B.

D. Bearings

In addition, the model can account for the operating-point-dependent impedance behavior of the motor's bearings. Hence, each bearing is modeled by introducing a R-$C_\mathrm{L}$circuit combined with a switch. Accounting for the bearings' specific impedance characteristic is particularly important when focusing on bearing currents in the analysis applying the model [12].

If the switch is open, the bearing behaves capacitively, which corresponds to high rotational speeds or hydrodynamic lubrication conditions. In contrast, if the switch is closed, the bearing is effectively short-circuited due to the very small resistance value. This represents metallic contact at low-speed or at standstill conditions where lubrication breaks down [12].

E. Parameterization

As outlined in [6], proper parameterization that accounts for rotor and magnetization current dependencies is essential. Furthermore, different FEM methods must be applied.

The frequency-dependent capacitances C and conductances G can only be determined through electrodynamic field simulation, while in complement, the R and L parameters must be derived with a special magnetodynamic FE-simulation to account for hysteresis and eddy current effects in the laminated core, as well as the influence of magnetization from rotor magnets. The detailed FE-methodology of the parameterization of each R-L-C-G-element is provided in [6].

For the Back-EMF extension introduced in this paper, three parameterization approaches are possible. The first approach involves an analytical method as described in [13]. Accordingly, the parameterization of the induced voltage from the rotor u_P is based on the air gap field, which is inherently linked to each coil of the winding. Following the methodology, the induced voltage of one phase can be analytically distributed to each coil side [13].

Alternatively, since in state-of-the-art motor development detailed flux maps, flux linkage and induced voltage in the windings are typically calculated using low-frequency (LF) electromagnetic field simulation, these results can be adopted directly. Based on the known angular position of a given coil side, its induced voltage can be computed as per [13], thereby completing the motor model's parameterization.

In another approach, a FE-simulation can be configured in such a way that each coil is modeled individually, allowing for the induced voltage to be calculated for each coil side from the LF field solution, considering the winding scheme.

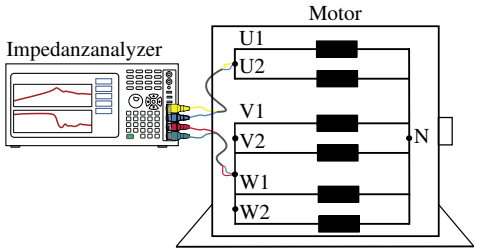

Fig. 3: Validation setup in DM-connection

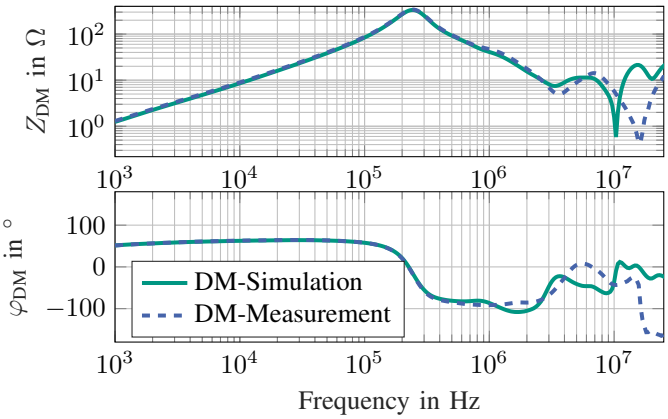

Fig. 4: Measurement and simulation result for the motor in DM setup

III. Validation

A. Impedance Measurement

The common validation method for HF-models in literature involves applying an impedance analyzer. Also for this study, as shown in Fig. 3, the differential mode (DM) configuration was employed, where phases V and W were short-circuited and measured in series with phase U using a *Keysight E4990A* impedance analyzer [14], within a frequency range of 1 kHz to 30 MHz.

The comparison between the measured and simulated results is presented in Fig. 4.Strong agreement between measurement and simulation can be observed, particularly up to 3 MHz. In the sub-resonant frequency range, the simulated behavior matches almost exactly, with the DM-impedance Z_{DM} being primarily dominated by the inherent inductive characteristics of the winding. Although the inductance parameterization value decreases with increasing frequency, Z_{DM} increases proportionally to the angular frequency ω. According to [15], the resonance at approx. 260 kHz, where the impedance peak occurs and the phase angle crosses zero, results from frequency-dependent current displacement and eddy current effects. Beyond this point, the impedance is dominated by the capacitances between the winding and the stator, as indicated by a phase angle φ_{DM} approaching $-90°$. The anti-resonance-point at approx.

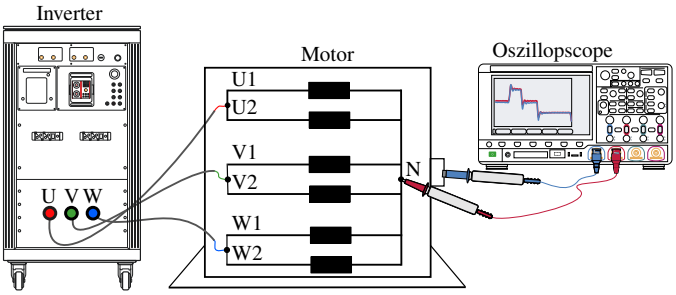

Fig. 5: Validation setup for CM measurements

B. Common-Mode Measurement

Since the impedance behavior of an electric machine derived from small-signal analysis differ widely from motor operation behavior, another validation method is necessary. According to the schematic measurement setup in Fig. 5 the machine under investigation was operated on a motor test bench with an Si-IGBT traction inverter under no-load conditions. This method is intended not only to validate the current-dependent parameterization of the HF-motor model, but also to ensure that the back-EMF is modeled correctly, as the rotor significantly influences the winding's impedance behavior, voltage stress, and other parasitic HF-effects [6].

Due to the accessibility of the neutral point and the rotor shaft, two additional measured variables were obtained. The CM-voltage at the neutral point was measured using a voltage probe, while the rotor shaft voltage was measured with a carbon brush. To accurately simulate real operating conditions, the measured phase voltages u_{U0}, u_{V0}, and u_{W0} at the motor terminals with reference to the housing potential were used as initial voltage conditions in the simulation model.

This approach eliminates the need for additional explicit modeling of the inverter and the motor supply cables, as their transient switching behavior is inherently captured in the initial conditions. The measurement and simulation results are shown in Fig. 6.

Overall, the simulation results closely match the voltage measurements at the machine's accessible neutral point of the machine u_{N} with a mean absolute percentage error $\mathrm{MAPE_N} = 2.62\,\%$, the voltage of the rotor shaft on the drive-end (DE) side $u_{\mathrm{shaft,DE}}$ with $\mathrm{MAPE_{shaft,DE}} = 2.22\,\%$ and the potential of the non-drive-end (NDE) side $u_{\mathrm{shaft,NDE}}$ with $\mathrm{MAPE_{shaft,NDE}} = 1.72\,\%$.

Finally, to validate the consistency between measurement and simulation at different operating points, the voltage drop between the motor's terminal and neutral point for each phase was calculated. The average error across all three phases is $\mathrm{MAPE_{UVW}} = 1.65\,\%$.

These results, in both, frequency and time domain, confirm that the model itself is not only appropriate and valid, but also demonstrate that all required frequency-dependent equivalent circuit elements were correctly parameterized. Therefore, the validated model will be used in the subsequent sensitivity

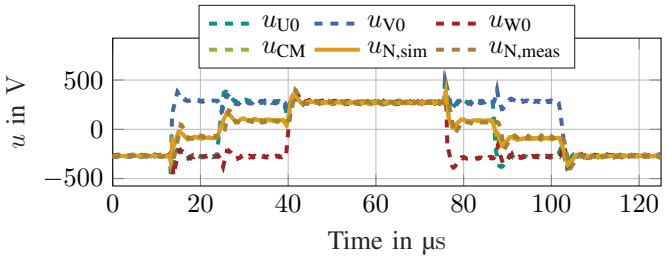

(a) Voltages at the terminal and neutral point of the motor

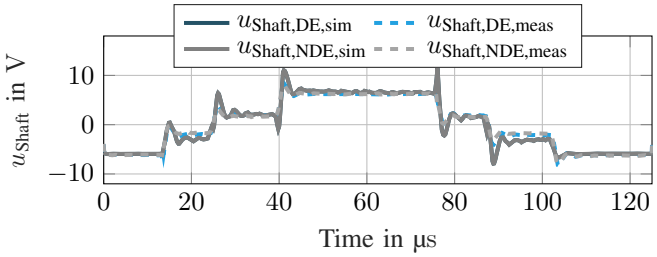

(b) CM voltage at the DE- and NDE- sides of the motor shaft

Fig. 6: Measured and simulated common-mode voltages at the motor terminal u_{CM}, neutral point u_{SP} and the DE-/NDE-side of the shaft $u_{shaft,DE/NDE}$

analysis to investigate the influence of assumptions and simplifications on the impedance behavior, inverter-related voltage distribution or other parasitic HF-effects.

IV. Sensitivity Analysis

A. Overhang

Most HF-models in the literature focus solely on the stator winding itself and often neglecting critical phenomena such as inter-turn effects, the impact of the rotor and its magnets, iron losses and hysteresis effects and in some cases also the end-winding region [1].

To investigate the impact of the overhang impedance Z_{WK} on the overall DM-impedance Z_{DM} of the motor, the own validated model was utilized, and the results are presented in Fig. 7.

The sensitivity analysis evaluates three scenarios in which Z_{WK} of the validated reference model is scaled between $1/10$ and $1/1000$. As depicted in Fig. 7, neglecting the overhang impedance results in an error of up to $15\,\%$. Since this

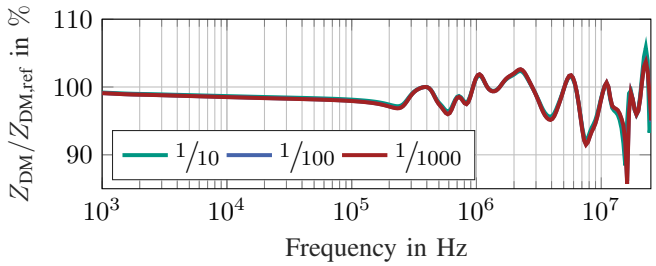

Fig. 7: Sensitivity on neglecting the overhangs' impedance

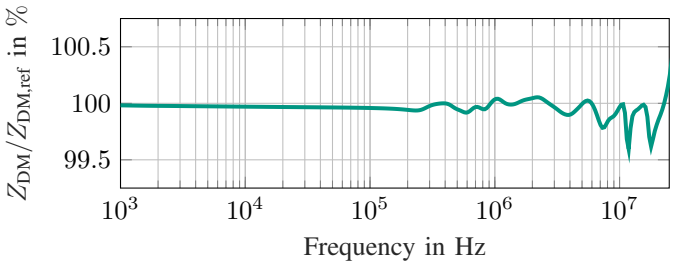

Fig. 8: Sensitivity on neglecting the overhangs' capacitances

error exceeds the measurement error range of an impedance analyzer, this analysis highlights the importance of considering the overhang impedance in HF-models.

Even when HF-models include the end-winding regions, the inter-winding capacitances in the overhangs are often neglected, as discussed in works such as e.g. [7], [16]. For the sensitivity analysis in this study, additional inter-winding capacitances for the end-winding region were introduced in the own model. Analogous to the previously discussed scenario, Fig. 8 shows the impact of neglecting these capacitances between the conductors, revealing that the associated error is less than $1\,\%$. This small error is primarily because the overhang region is surrounded by air, and the capacitances dominating the impedance at high frequencies are located within the stator lamination part. Additionally, the capacitance between two conductors in the overhang of hairpin windings is typically very small due to the large spacing between the conductors. In accordance with [17], overhang capacitances account for merely $3\,\%$ of the total motor capacitances. This simplification offers considerable advantages for the simulation modeling process, as it considerably reduces the complexity of the model. In particular, it eliminates the necessity to model the exact geometry and conductor positioning in the bending and welding regions of the overhang.

B. Back-EMF

In the analysis of HF-behavior during real motor operation at a specific operating point, rather than performing a small signal impedance analysis, accounting for the rotor's back Back-EMF becomes crucial. This can be demonstrated by evaluating the voltage drop between the motor terminal and the neutral point. The base for this investigation is the validation result presented in Section III-B.

To substantiate this hypothesis, Fig. 9 shows the measured phase voltage drop and the error between simulation and measurement for both cases, with and without Back-EMF consideration, for all three phases.

Neglecting the Back-EMF results in significant discrepancies between the simulated and measured phase voltage drop, with errors exceeding $25\,\mathrm{V}$, as shown in Fig. 9b. In contrast, the error plot presented in Fig. 9c, which takes the Back-EMF into account, does not exceed an absolute value of $2\,\mathrm{V}$.

Moreover, it is important to note that this discrepancy corresponds only to the specific electrical period at low rotational

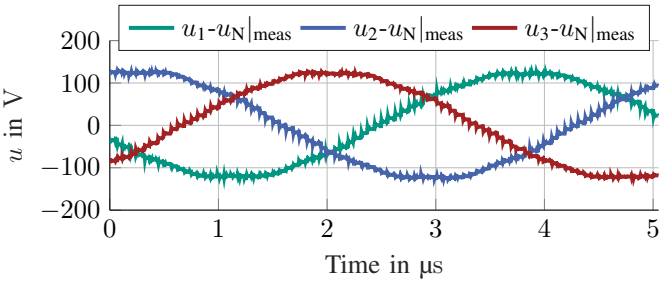

(a) Measured phase voltage drop

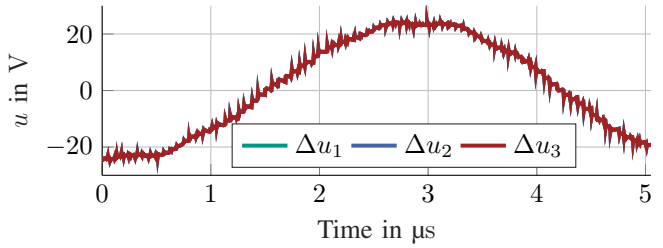

(b) Error of phase voltage drop without Back-EMF consideration

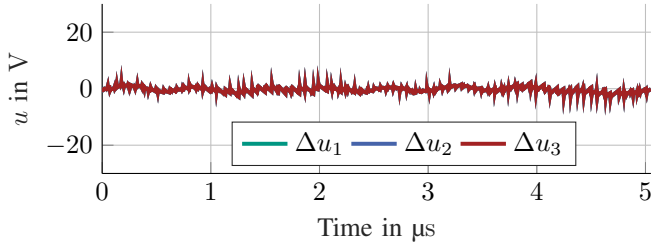

(c) Error of phase voltage drop with Back-EMF consideration

Fig. 9: Measured phase voltage drop and error between simulation and measurement regarding the Back-EMF consideration

speeds considered here. As rotational speed increases, the Back-EMF proportion in phase voltage rises, leading to even larger errors.

The importance of accounting for the Back-EMF becomes even more evident when analyzing the maximum voltage load experienced by each coil-side over the entire electrical period, as depicted in Fig. 10. The results indicate that neglecting Back-EMF leads to an underestimation of the maximum voltage. Although the maximum voltage difference at the investigated operating point is only $4.38\,\%$, simulations at higher speeds, where the Back-EMF has more significant impact, show errors exceeding $40\,\%$.

Without an additional proof given here, the Back-EMF impact is mirrored in the insulation stress analysis between two coil-sides. In this analysis, however, the opposite effect is observed. Introducing the Back-EMF reduces the insulation stress, as it exerts a symmetrizing effect on the winding, elevating the base voltage level and thereby reducing the differential voltage between adjacent conductors within one slot.

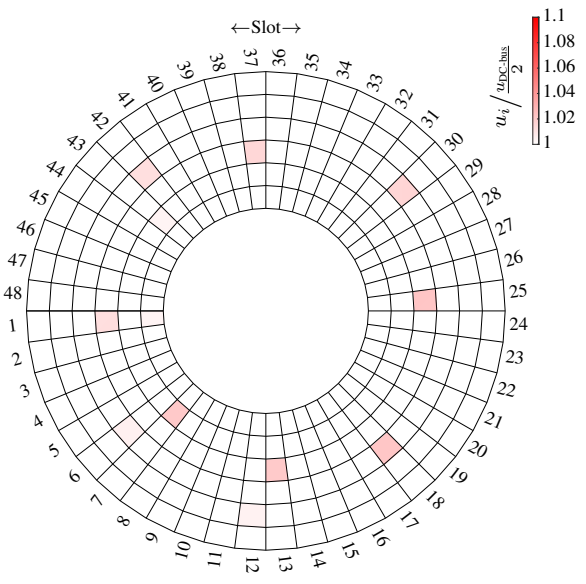

(a) Maximum voltage of each coil-side without Back-EMF consideration

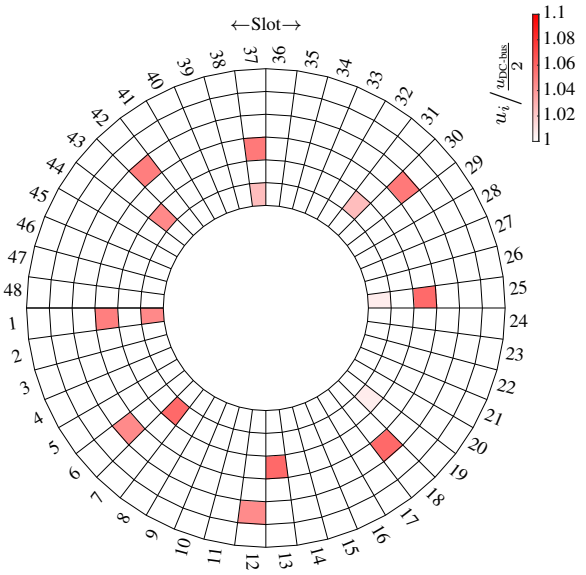

(b) Maximum voltage of each coil-side with Back-EMF consideration

Fig. 10: Maximum voltage of each coil-side during an electric period normed on half of the DC-bus voltage

C. Inverter switching state

Analyzing the real motor operation also requires the consideration of the motor's terminal connections, which can vary depending on the analysis mode.

In a typical two-level PWM-modulated three-phase inverter, phase voltage and phase lags are set on average only, using the discrete values of its DC-bus voltage and a function of the voltage space vector. Consequently, the motor terminals are

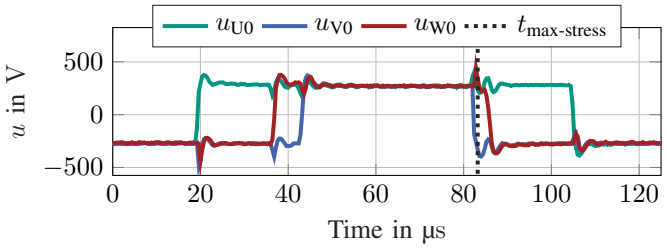

Fig. 11: PWM-period and point in time where the maximum insulation stress occurs

subjected to only eight distinct voltage states, given in Table I. Since four states are an inverse of the others, the number of unique modes that must be modeled is reduced to four [18].

Switching state	*Phase 1*	*Phase 2*	*Phase 3*
1	-1	-1	-1
2	+1	-1	-1
3	-1	+1	-1
4	-1	-1	+1
5	-1	+1	+1
6	+1	-1	+1
7	+1	+1	-1
8	+1	+1	+1

TABLE I: Switching states of a classic two-level pulse inverter

As discussed in [19], [20], the maximum CM load of the motor occurs if the modulation index is zero, so that all three-phase half bridges switch simultaneously to the same state at the same time.

However, in terms of insulation stress, a zero modulation index does not necessarily represent the worst-case scenario. Due to the results of this sensitivity analysis, it is essential to analyze every switching state. Moreover, additional overvoltages and other high-frequency effects can occur in one phase while switching another half bridge.

Furthermore, regarding coil-pitch windings, coil sides from different phases may share a slot. In cases where these conductors forced to inverse switching states, the differential voltage and consequently, the insulation stress between these conductors can be significantly higher.

The results after simulating all switching state of Table I indicate that the maximum insulation stress occurs during a switching event from state 8 to state 6. The corresponding PWM-period and the specific point in time are highlighted in Fig. 11.

During this PWM-period, the maximum insulation stress reaches $2.94 \cdot u_{\text{DC-bus}}$. In contrast, when all switching states are identical, the maximum insulation stress is only $1.27 \cdot u_{\text{DC-bus}}$. For the more detailed comparison, Fig. 12 presents the maximum insulation stress between two coil-sides of all layers in both scenarios.

In addition, already from Fig. 11 can be observed that as soon as one half-bridge switches, a transient voltage overshoot is induced in the other phases due to mutual HF-couplings, leading to additional overall insulation stress. Therefore, it

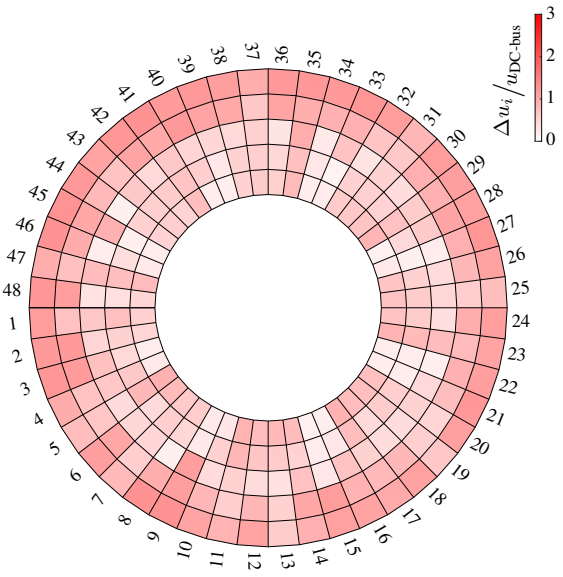

(a) Maximum insulation stress of each layer for $mi = 0$ or switching states 1 or 8

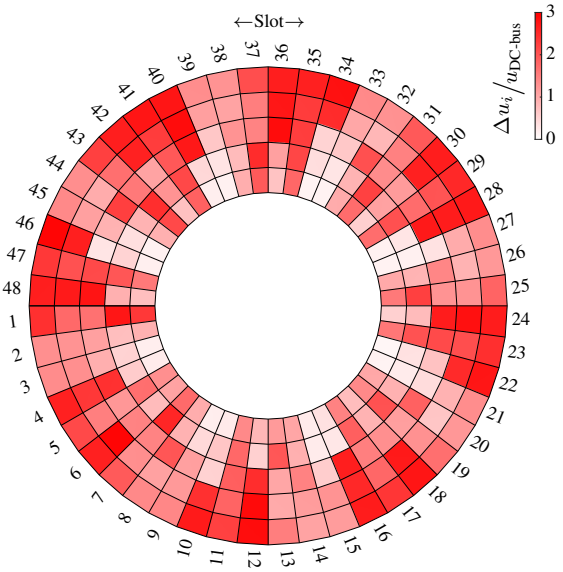

(b) Maximum insulation stress of each layer for $mi \neq 0$

Fig. 12: Maximum voltage of each coil-side during an electric period normed on the DC-bus voltage

can be concluded that it is crucial to account for the exact voltage switching behavior of the motor-inverter combination, to accurately assess and consider the insulation stress in motor insulation design.

V. Summary

In conclusion, this study presents a sensitivity analysis to investigate the impact of various common simplifications and

assumptions in HF-modeling.

The analysis focuses on the effects of neglecting the overhang impedance, capacitive couplings in the end-windings, Back-EMF, and inverter switching states on the motor's overall impedance, voltage distribution, and insulation stress.

The results show that neglecting the overhang impedance in HF-models can lead to significant errors, exceeding the measurement error tolerances of standard impedance analyzers. While modeling the overhang impedance itself is essential for accurate modeling, neglecting the inter-winding capacitances simplifies the model with minimal impact on accuracy.

Additionally, a novel approach is introduced in this study that considers the Back-EMF into the HF-model, extending its applicability to real operational conditions and operating point dependency. Neglecting the Back-EMF leads to substantial errors in phase voltage drop, voltage distribution and insulation stress, not only for real motor operation analysis, but also impedance analysis are influenced by the rotor magnets, as shown in [6]. The importance of the Back-EMF consideration becomes even more significant as motor speed increases, due to the rising magnitude of induced voltage. Finally, the study reveals that maximum insulation stress in the motor occurs during specific PWM-switching events and not necessarily at a zero modulation index. Moreover, the necessity of modeling the exact inverter switching behavior in HF-motor models to accurately assess electrical stress is highlighted.

For future work, the development of a comprehensive calculation and analysis routine is suggested to improve the efficiency of the proposed method. This would allow for a detailed analysis of each operating point in electric machines with respect to parasitic effects, similar to efficiency map calculations and enhance the development process of electric machines in regard to electric stress.

REFERENCES

[1] Y. Moreno, G. Almandoz, A. Egea, B. Arribas, and A. Urdangarin, "Analysis of permanent magnet motors in high frequency—a review," vol. 11, no. 14, p. 6334, 2021, pII: app11146334.

[2] S. Niedzwiedz, S. Frei, M. Obholz, and J. Heyen, *Analyse leitungsgeführter Emissionen im HV-Bordnetz von elektrischen Fahrzeugen*. Aachen : Apprimus, 2016.

[3] S. Scheuermann, M. Doppelbauer, B. Hagemann, A. Jarosz, and B. Schmitz-Rode, "Validation of a slot-based high-frequency model of a hairpin winding stator in time-domain," in *2022 International Conference on Electrical Machines (ICEM)*. IEEE, 2022, pp. 1648–1654.

[4] S. Scheuermann, M. Doppelbauer, B. Hagemann, A. Jarosz, and F. Hoffmann, "Investigation of winding schemes by slot-based high-frequency modelling of a hairpin winding stator," in *11th International Conference on Power Electronics, Machines and Drives (PEMD 2022)*. Institution of Engineering and Technology, 2022, pp. 520–525.

[5] J. E. Ruiz-Sarrio, F. Chauvicourt, and C. Martis, "Sensitivity analysis of a numerical high-frequency impedance model for rotating electrical machines," in *2022 International Conference on Electrical Machines (ICEM)*, 2022, pp. 1260–1266.

[6] S. Scheuermann, M. M. Brodatzki, and M. Doppelbauer, "Investigation of the parameterization influence in high-frequency models for traction motors with hairpin windings," in *IECON 2024- 50th Annual Conference of the IEEE Industrial Electronics Society*, 2024.

[7] G. Berardi, S. Nategh, and N. Bianchi, "Inter-turn voltage in hairpin winding of traction motors fed by high-switching frequency inverters," in *2020 International Conference on Electrical Machines (ICEM)*. IEEE, 2020, pp. 909–915.

[8] A. Mütze, *Bearing currents in inverter fed AC motors*, ser. Berichte aus der Elektrotechnik. Shaker, 2004.

[9] Mäki-Ontto, Petri, 1971-, "Modeling and reduction of shaft voltages in ac motors fed by frequency converters," 2006.

[10] A. Muetze and A. Binder, "Don't lose your bearings," vol. 12, no. 4, pp. 22–31, 2006.

[11] O. N. Magdun, *Calculation of High-Frequency Current Distributions in Inverter-Fed Electrical Machines*, 1st ed., ser. Berichte aus der Elektrotechnik. Shaker, 2013, magdun, Oliver Narcis (Verfasser).

[12] S. Scheuermann, M. Doppelbauer, B. Hagemann, A. Jarosz, J. Kett, and J. Stoß, "Development of a bearing test bench to investigate root causes of bearing current damages," in *2023 IEEE International Electric Machines & Drives Conference (IEMDC)*. IEEE, 2023, pp. 1–5.

[13] G. Müller and B. Ponick, *Theorie elektrischer Maschinen*, 6th ed., ser. Elektrische Maschinen. Wiley-VCH, op. 2009, vol. 3.

[14] Keysight Technologies. (2022) N28xxa/b passive probes. [Online]. Available: https://www.keysight.com/de/de/assets/7018-02806/data-sheets/5990-7111.pdf

[15] H. Kaden, *Wirbelströme und Schirmung in der Nachrichtentechnik*, zweite vollkommen umgearbeitete auflage ed., ser. Klassiker der Technik. Springer Berlin Heidelberg and Imprint: Springer, 2006, kaden, Heinrich., (author.).

[16] S. Sundeep, J. Wang, and A. Griffo, "Holistic modeling of high-frequency behavior of inverter-fed machine winding, considering mutual couplings in time domain," *IEEE Transactions on Industry Applications*, vol. 57, no. 6, pp. 6044–6057, 2021.

[17] K. Vostrov, J. Pyrhonen, and J. Ahola, "The role of end-winding in building up parasitic capacitances in induction motors," in *2019 IEEE International Electric Machines & Drives Conference (IEMDC)*. IEEE, 2019, pp. 154–159.

[18] F. Jenni and D. Wüest, *Steuerverfahren für selbstgeführte Stromrichter*. vdf Hochschuvlerag AG, 1995.

[19] J. Austermann, *Rückspeisestromrichter mit geregeltem Zwischenkreisstrom*, [1. auflage] ed., ser. Berichte aus der Elektrotechnik. Shaker Verlag, 2018, austermann, Johann (Verfasser).

[20] P. Hillenbrand, S. Tenbohlen, C. Keller, and K. Spanos, "Understanding conducted emissions from an automotive inverter using a common-mode model," in *2015 IEEE International Symposium on Electromagnetic Compatibility (EMC)*. IEEE, 2015, pp. 685–690.